Linear and nonlinear crystal optics using the magnetic field of light

Zachary N. Buckholtz and Deniz D. Yavuz

Phys. Rev. A **101**, 023831 — Published 18 February 2020

DOI: 10.1103/PhysRevA.101.023831

Linear and Nonlinear Crystal Optics Using the Magnetic Field of Light

Zachary N. Buckholtz and Deniz D. Yavuz

Department of Physics, 1150 University Avenue,

University of Wisconsin at Madison, Madison, WI, 53706

(Dated: January 30, 2020)

Abstract

We study the ${}^7F_0 \rightarrow {}^5D_1$ magnetic-dipole transition in the $4f$ shell of europium ions at a wavelength of 527.5 nm and demonstrate spectral hole burning, ion class selection, and optical pumping to specific ground hyperfine states. We then use the narrow lines of the selected ions to observe linear group delay of a weak probe pulse with a group velocity of $c/3800$. We also demonstrate electromagnetically induced transparency by establishing a Λ scheme between the ground hyperfine levels and driving the ions to a dark state.

PACS numbers: 42.70.-a, 78.20.Ci, 42.65.An, 81.05.Xj

I. INTRODUCTION

It is well-known that natural materials almost always primarily interact with light through its electric field. This is because, due to fundamental constants of nature, the interaction with the magnetic field is typically weaker by five orders of magnitude. One immediate consequence of this is that, while studying optical interactions, researchers generally take the permeability of the material to be equal to its free space value ($\mu = \mu_0$).

The weakness of the magnetic response is a critical limitation for optical device applications. For example, to achieve a negative refractive index, both the permittivity and the permeability of the material need to be significantly modified; i.e., the material needs to interact strongly with both the electric and the magnetic fields of light [1–8]. Over the last two decades, new types of materials that show magnetic response in the optical region of the spectrum have been invented and continually refined [9–13]. These materials, referred to as metamaterials, use periodic structures to induce a magnetic-dipole response (typically in addition to an electric-dipole response) over a certain range of wavelengths. Metamaterials traditionally utilize all metal or metal/dielectric structures which can be engineered using a variety of nanolithography techniques. Over the last five years, there has also been important progress in constructing all-dielectric metamaterials utilizing Mie resonances in high-refractive index nanoresonators [15–17]. All-dielectric metamaterials are optically transparent and do not suffer from the large ohmic losses associated with metal-based devices.

It was recognized early on that it may also be possible to construct negative index materials using sharp transitions of atoms or ions [18–26]. Instead of relying on engineered patterns, the idea is to utilize the resonances provided to us by nature. Similar to the early stages of structured metamaterial research, obtaining a large magnetic response and modifying the permeability has remained the key challenges of this approach. In this article, we use a europium doped crystal (specifically europium doped yttrium ortho-silicate, Eu:YSO) and demonstrate, for the first time, coherent control of the permeability in a bulk optical crystal. We achieve this by utilizing the $^7F_0 \rightarrow {}^5D_1$ purely magnetic-dipole transition in the $4f$ shell of europium ions at a wavelength of 527.5 nm [27]. We first use this transition to demonstrate spectral hole burning and ion class selection under the broad (GHz wide) inhomogeneous profile. This allows the creation of narrow (MHz-wide) magnetic-dipole op-

tical absorption resonances with multiple stable ground hyperfine states. The selected ions can be optically pumped to any of the ground states, and both linear and nonlinear optical interactions with the incident beams can then be observed. Using these narrow lines, we demonstrate a linear group delay with a group velocity of $c/3800$ for a weak, 0.5-μs-long optical pulse. We also demonstrate electromagnetically induced transparency (EIT) using probe and coupling laser beams in a Λ configuration [28–30]. EIT is a nonlinear optical phenomenon in which the transmission of the probe beam is modified by the presence of the coupling beam. It is achieved by driving the ions into the dark state and establishing a Raman coherence between the hyperfine levels.

The level of control of the permeability that we demonstrate in this article is not currently sufficient to achieve a negative refractive index. With spectral hole burning we can produce a magnetic susceptibility (and therefore permeability) at the level of $\chi_M \approx 10^{-5}$, and using EIT we can coherently control this susceptibility at the level of $\Delta\chi_M \approx 10^{-6}$. However, as we will discuss in the conclusions, there are many avenues for extending these proof-of-principle results to give a larger magnetic response. We also note that, using chirality, a magnetic susceptibility at the level of $\chi_M \approx 10^{-2}$ is sufficient to achieve a negative refractive index [22–24].

The atomic approach to metamaterials that we focus on in this article has important advantages over structured devices. Metamaterials require an optical response which is uniform on wavelength spatial scales, and the granularity of the periodic structures is a fundamental limitation for device performance. As shown in Fig. 1, due to resolution limitations of lithographic techniques, current metal-based metamaterials are limited to feature scales of about 100 nm (i.e., about $\lambda/5$ in the optical region of the spectrum). In all-dielectric metamaterials, Mie resonances require spheres or cylinders of specific sizes, which fundamentally sets the feature scale to a similar range of $\lambda/2$ to $\lambda/5$. The large feature size results in key limitations to the device performance. For example, "perfect lenses" constructed using current metamaterials would be limited to a resolution of about $\lambda/5$. In contrast, when atomic transitions are utilized, the unit-cell length of the crystal sets the scale for feature size since the individual emitters are atomic ions. The unit-cell dimensions of the host crystal that we utilize, yttrium ortho-silicate (YSO), is also shown in Fig 1. Even at low doping concentrations of order 0.1%, the spacing between radiating ions is about 10 nm, which results in uniformity of order $\lambda/50$.

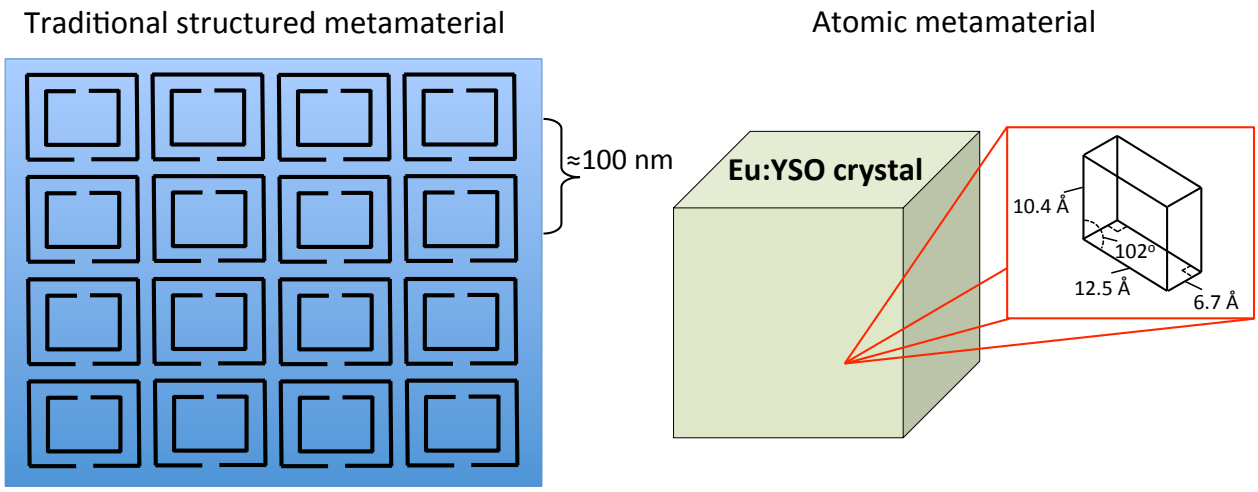

FIG. 1: A traditional engineered metamaterial, such as the double split-ring resonator structure shown on the left, utilizes periodic structures with a feature size of about 100 nm. In contrast, when atomic transitions are utilized, the unit-cell length of the crystal sets the scale for feature size since the individual emitters are atomic ions. The unit-cell dimensions of the crystal that we utilize, europium doped yttrium ortho-silicate (Eu:YSO), is shown on the right. Since the feature size sets a fundamental limitation of the device performance, this means that atomic metamaterials have an advantage over structured metamaterials.

Another restriction of structured metamaterials is that their magnetic response is limited to a fraction of the plasma frequency [31]. This limits the highest frequency (and therefore the shortest wavelength) that negative refraction can be achieved to somewhere in the middle of the visible region of the spectrum. In contrast, as we will discuss in the conclusions section, there are realistic prospects for extending the experiments described here to shorter wavelengths by using magnetic dipole transitions of rare-earth ions in the ultraviolet region of the spectrum.

II. RARE-EARTH DOPED CRYSTALS

Although the existence of magnetic dipole transitions have been known for some time [32, 33], accessing these transitions is challenging, especially in a solid. As mentioned above, the

oscillator strengths of these transitions are weaker by a factor of α^2 (the quantity $\alpha \approx 1/137$ is the fine structure constant) compared to electric dipole transitions. As a result, these transitions are easily dwarfed by nearby electric-dipole transitions or are largely broadened by dissipative processes. The electrons in the open $4f$ shell of rare-earth ions in doped crystals form a special environment where these challenges can be overcome [34–38]. The $4f$ shell is shielded by the filled $5s$ and $5p$ shells and interacts weakly with the crystal environment. As a result, the intra-configurational $4f \rightarrow 4f$ transitions are sharp, and they are very much like free-ion transitions that are only weakly perturbed by the crystal field. The homogeneous linewidths of the optical $4f \rightarrow 4f$ transitions can be very narrow, even at the Hz level at cryogenic temperatures. Furthermore, hyperfine states of the ground level are stable and long-lived, and they can be used to induce Raman transitions. There is still an inhomogeneous broadening due to the interaction with the crystal field, which is typically at the GHz level. This broadening is unusually small for a solid environment, which is again a result of the $4f$ shell being weakly perturbed by the crystal field.

Due to the richness of the electronic structure, magnetic-dipole transitions in the optical region can be found within the $4f$ shell. The transition that we use, ${}^7F_0 \rightarrow {}^5D_1$ of the Eu^{+3} ions has recently emerged as a workhorse in studying optical magnetic response. About three years ago, Novotny and colleagues demonstrated laser excitation of this transition [39]. They utilized a tightly-focused radially polarized laser, which produced unique spatial profiles for the electric and magnetic fields at the focus. By imaging the excitation profile of europium-doped nanoparticles at room temperature, they conclusively demonstrated the magnetic-dipole nature of this transition. We recently observed strong-field Rabi flopping on this transition at cryogenic temperatures [40]. Using angle-dependent fluorescence, we also confirmed that the electrons interacted with the magnetic field of light as they were being excited. On related work, the manipulation of magnetic dipole emission from europium ions near dielectric surfaces was very recently studied in Ref. [41]. In other pertinent prior work, we would like to note the pioneering work of Rand and colleagues [42–45]. They have discovered an unusually large magnetic optical response using femtosecond lasers at moderately high intensities of $\sim 10^8$ W/cm^2, both in dielectric liquids [42, 43] and molecular crystals [44, 45]. The physical mechanism for this magnetization is the applied magnetic torque on the induced polarization causing molecular rotations in the strong field regime.

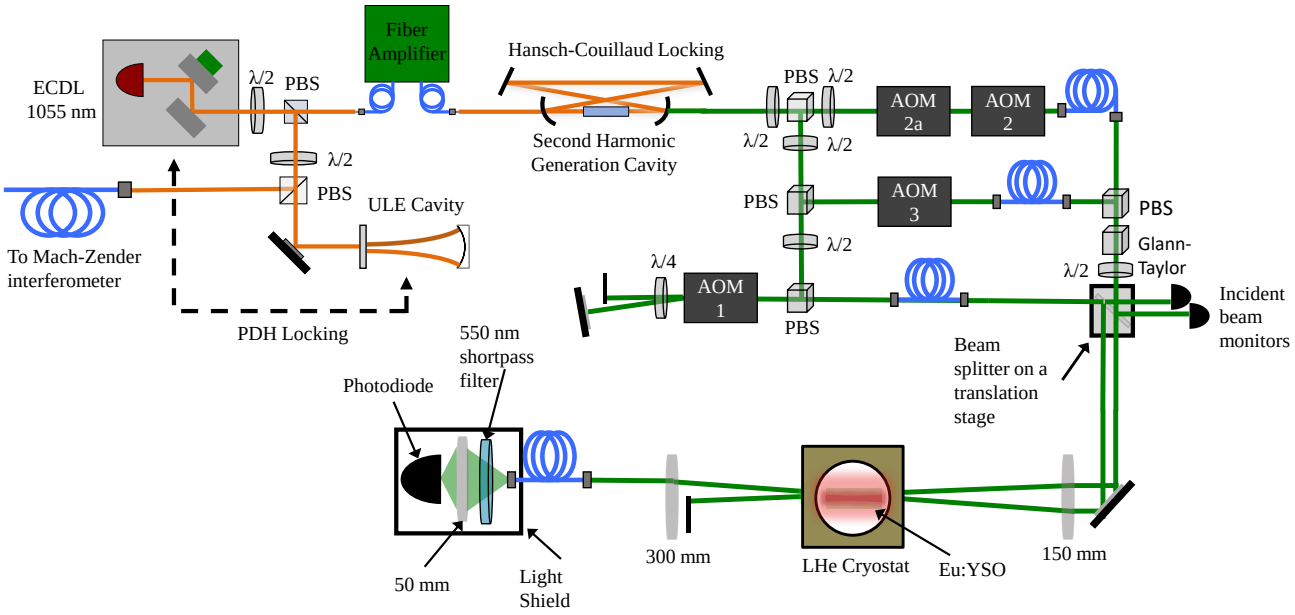

FIG. 2: The experimental schematic. We begin with a 1055 nm ECDL locked to a ULE reference cavity and whose linewidth is monitored by a Mach-Zender interferometer. The beam is then amplified by a fiber amplifier, and frequency doubled in a PPKTP based ring cavity. The 527.5 nm light output is split into three beams, the probe, coupling, and repump beam. The timing, power, and frequency of the three beams are controlled by AOMs. The coupling and repumper beams are then overlapped while the probe beam propagates parallel to them but displaced by 2 mm. The parallel beams are then focused into the crystal at a small enough angle that they are overlapped within the 1 cm crystal. After the crystal, the coupling and repumper beams are blocked. The probe beam is sent through a fiber into an enclosed box to block scattered light. After leaving the fiber, the probe beam is passed through a 550 nm shortpass filter to block fluorescence from the crystal and then focused onto a photodiode for detection. ECDL: external-cavity diode laser, PBS: polarizing beam splitter, ULE: ultra-low expansion, PDH: Pound-Drever-Hall, AOM: acousto-optic modulator, $\lambda/2$: half-wave plate, $\lambda/4$: quarter-wave plate.

III. EXPERIMENTAL SCHEMATIC

A simplified schematic of our experiment is shown in Fig. 2. The $^7F_0 \rightarrow {}^5D_1$ transition wavelength is 527.5 nm (green) and our laser system starts with an infrared 1055 nm

external cavity diode laser (ECDL). We use an ultra-low expansion (ULE) glass cavity as a frequency reference. The ECDL is locked to one of the axial modes of the cavity that lies near the peak of the inhomogeneous profile. Locking reduces the absolute linewidth of the ECDL to ≈100 kHz, which is continually monitored using a fiber-based Mach-Zender interferometer (not shown in Fig. 2). The long-term (over several days) absolute frequency drift of the modes of the cavity is at the 100 kHz level. The frequency stabilized ECDL output is amplified to an optical power exceeding 5 W using a ytterbium-doped fiber amplifier. We frequency-double the fiber amplifier output using second harmonic generation with a periodically-poled KTP (PPKTP) crystal. To increase the efficiency of the generated second harmonic, we utilize a ring cavity, which is locked to the fundamental beam at 1055 nm.

The green output from the doubling cavity is then split into three beams which we call the probe, the coupling, and the repumper. As we will discuss below, these three beams are used for spectral hole burning, ion-class selection, optical pumping, and EIT. Each beam goes through an acousto-optic modulator (AOM) for precise frequency and timing control. The probe beam AOM uses a double-passed configuration to achieve a wider tuning range of the probe frequency with relatively little variation of its power. Each beam is spatially filtered through a single mode fiber (not shown in Fig. 2) before they are combined and focused inside the Eu:YSO crystal. The spot size of the beams at the focus is $W_0 = 45$ μm ($1/e^2$ intensity radius). The probe laser crosses the other two beams at an angle of 15 mrad for ease of detection after the crystal. We use a 10-mm-long Eu:YSO crystal which is housed in a continuous-flow liquid helium cryostat to cool to a temperature of 4.5 K. Cooling is needed to reduce phonon-induced relaxation rates which critically determines homogeneous optical linewidths.

IV. SPECTRAL HOLE BURNING

Our spectral hole burning technique is similar to what has been previously achieved using forced electric-dipole transitions [46–49]. The key difference is that ions interact with the magnetic field of light instead of the electric field. The low-lying electronic levels of the $4f$ shell of Eu^{+3} are shown in Fig. 3(a) (the full $4f$ electronic configuration covers over 100,000 cm^{-1}). Our crystal is doped at $\sim 0.1\%$ with natural abundance europium, containing

48% ^{151}Eu and 52% ^{153}Eu. Each of these isotopes has a nuclear spin of $I = 5/2$. Eu^{+3} ions can occupy two unique sites in the YSO matrix, referred to as "site 1" and "site 2". For our experiments we select and use a class of the ^{153}Eu ions occupying site 2. The dominant contribution to the homogeneous linewidth of the $^7F_0 \rightarrow {}^5D_1$ transition is non-radiative, phonon induced relaxation of the excited $^5D_1$ level to $^5D_0$. This rate is $\Gamma = 2\pi \times 4.8$ kHz, corresponding to a non-radiative lifetime of $\tau = 33$ μs. The inhomogeneous linewidth of this transition is 1.6 GHz [40].

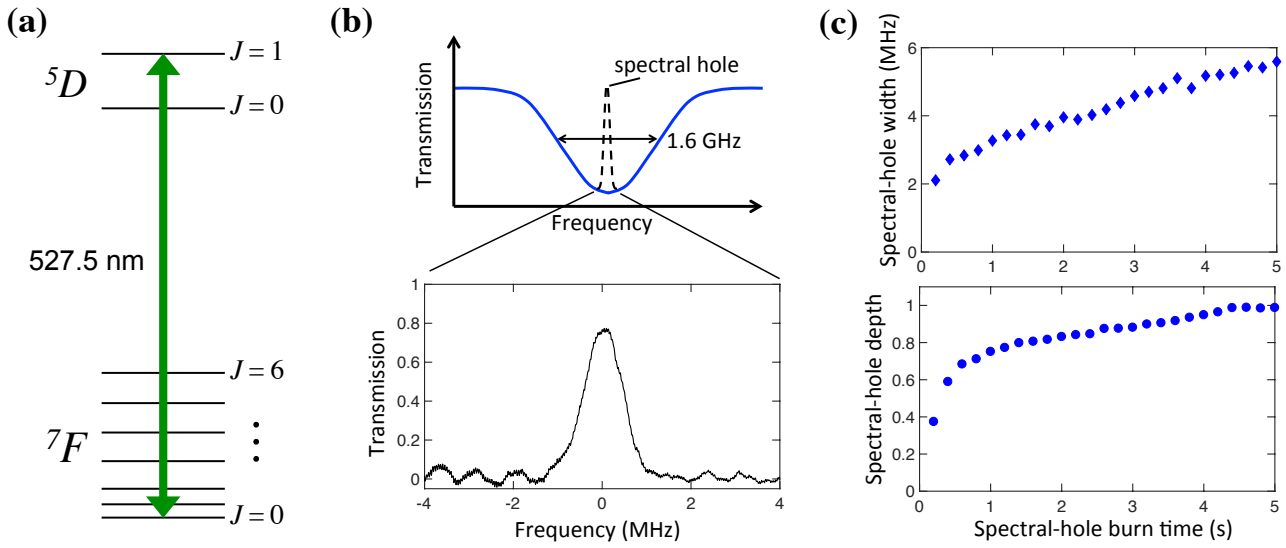

FIG. 3: (a) The levels of the $4f$ shell of Eu^{+3} ions with an energy below 20,000 cm^{-1}. The $^7F_0 \rightarrow {}^5D_1$ magnetic dipole transition is at a wavelength of 527.5 nm, has a homogeneous linewidth of $\Gamma = 2\pi \times 4.8$ kHz (due to phonon-induced relaxation), and is inhomogeneously broadened to 1.6 GHz due to variations in the crystal field. (b) Schematic description of a spectral hole and an actual experimental trace showing a spectral hole with a width of 2 MHz and a depth of 0.8. (c) The width and depth of a spectral hole as a function of burn-time for a burn-laser intensity of 40 mW/cm^2.

As shown in Fig. 4(a), the nuclear spin results in three hyperfine states, in both the ground and excited levels, labeled $|\pm 1/2\rangle$, $|\pm 3/2\rangle$, and $|\pm 5/2\rangle$ (while the spacing of the hyperfine states in the excited level is known, their ordering is not). The frequency spacings between the hyperfine states is smaller than the inhomogeneous profile. As a result, a single laser beam tuned close to the center of the inhomogeneous line couples to $3 \times 3 = 9$ different

transitions, each associated with a separate ion class. If the laser interacts with the ions for a sufficiently long amount of time, each ion class is optically pumped to ground hyperfine states that are not resonant with the laser beam. This establishes a spectral hole in the inhomogeneous profile, which is schematically shown in Fig. 3(b). Since the ground hyperfine levels are stable, the spectral hole lifetimes are quite long. We have observed lifetimes as long as one hour, but spectral holes in a rare-earth doped system are known to persist even for days at cryogenic temperatures [34]. Once a spectral hole is produced, it can be probed by applying a subsequent weak laser beam whose frequency is scanned. Figure 3(b) shows the transmission of such a laser as its frequency is scanned across the established spectral-hole. We routinely observe spectral hole widths at the 1 MHz scale.

If the frequency of the subsequent probing laser is scanned across the whole inhomogeneous profile, the full observed spectral-hole spectrum is rather complex [49]. The central spectral hole is accompanied by $2 \times 9 \times 9 = 162$ holes and anti-holes (the factor of 2 is due to the presence of the two isotopes) in the absorption spectrum. The holes and anti-holes appear at specific frequencies which are related to the hyperfine spacings. The depths of these holes and anti-holes are determined by the transition strengths between various hyperfine transitions. A detailed study of this complex hole and anti-hole spectra is left for a future publication.

Figure 3(c) shows the full-width-at-half-maximum (FWHM) and also the depth (fractional transmission) of the produced central hole as a function of the duration of the hole-burning laser. This data is taken for a hole burning laser with a power of 1 μW (the beam intensity at the focus is 40 mW/cm^2).

V. ION CLASS SELECTION

Figure 4(a) shows the energy levels and the three involved laser beams that we use for ion class selection and also for EIT. As mentioned above, each laser beam addresses 9 different classes of ions under the broad inhomogeneous profile. However, there is only one ion class shown in Figure 4(a), for which all three hyperfine ground states are coupled to an excited hyperfine level with one of the lasers. All other ion classes have at least one ground hyperfine state which is not connected to an excited hyperfine level. As a result, when all three laser beams are turned on, all the other ion classes are optically pumped to a non-addressed

hyperfine ground state and are therefore rendered "dark". Only the specific ion class with the frequencies and resonances shown in Fig. 4(a) keeps interacting with the beams, a process that is referred to as ion class selection.

We note that there are additional degeneracies that are not explicitly shown in Fig. 4(a). Each hyperfine level, which is shown in Fig. 4(a), actually consists of two values of the nuclear spin. For example, the highest energy hyperfine level in the ground level has a degeneracy of two with nuclear spin numbers $|+1/2\rangle$ and $|-1/2\rangle$, respectively. As a result, the total number of states in the ground level is $3 \times 2 = 6$. While this complicates optical pumping, to our knowledge, there aren't any strict selection rule that prohibits the excitation of any of these six states to the excited level. As a result, we do not expect any of these six states to be strictly dark. While coupling of some of these states could be weaker due to a smaller value of the matrix element, because ion class selection procedure occurs over quite-long time scales (many seconds), the system can be assumed to be closed.

For ion class selection, spectral-troughs (instead of holes) are preferred, in order to initially select ions that are resonant over a sufficiently broad region of the inhomogeneous profile. This reduces the interference of other ion classes with nearby resonance frequencies. Spectral troughs can be burned by scanning the frequency of the involved beams during the ion class selection process. An example spectral-trough which is about 14 MHz wide is shown in Fig. 4(b). Figure 4(c) shows the timing diagram for the experiments that will be discussed below. We follow a procedure which is similar to what was discussed in Refs. [47] and [49] where the authors investigated relative transition strengths between hyperfine levels for the forced electric dipole transitions in Pr^{+3} and Eu^{+3}.

Our ion-class selection procedure has four distinct steps. In the first step, we turn on the three beams at low optical powers (about 10 μW), continually scanning their frequencies over a range of 10 MHz at a rate of about 100 Hz. This is the ion-class selection process which continues for a time duration of about 3 s. In the second step, the repumper beam is turned off while the probe and coupling lasers are left on with their frequencies scanned. This step optically pumps all the ions in the selected class to the middle hyperfine ground state $|\pm 3/2\rangle$ (the state addressed by the repumper laser). In the third step, the coupling and repumping laser beams are turned on at a certain frequency to optically pump ions near that frequency to the $|\pm 1/2\rangle$ ground hyperfine state (i.e., to the state addressed by the probe laser beam). This creates a narrow, ≈ 1 MHz wide, absorption resonance for the

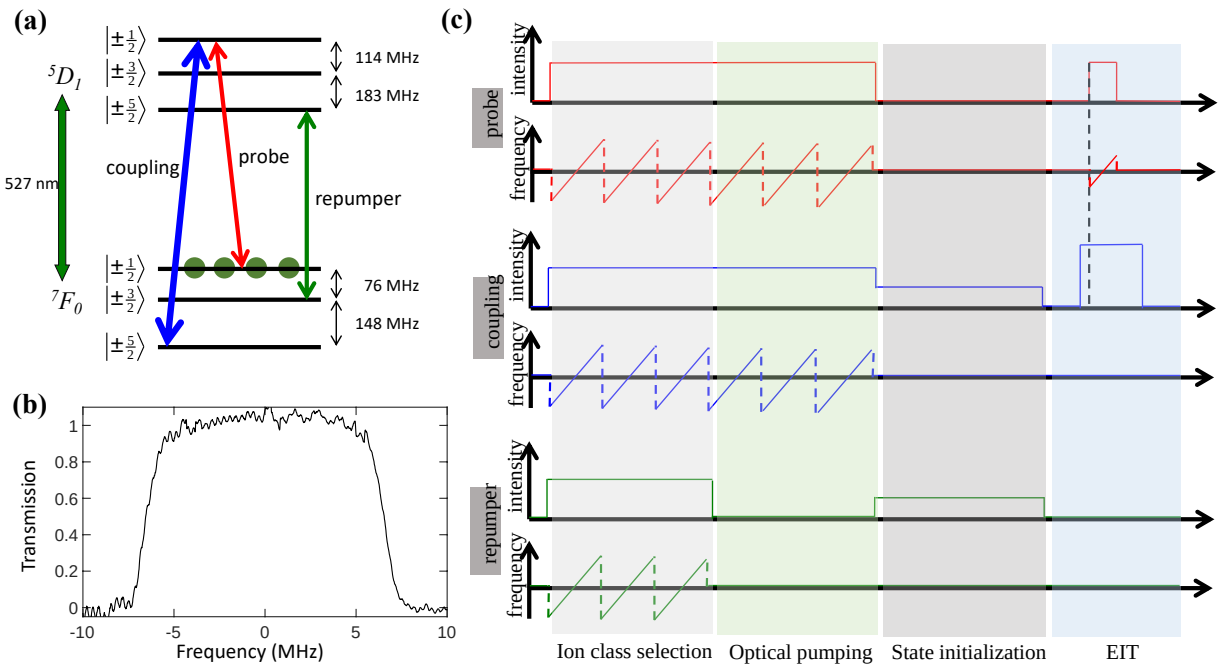

FIG. 4: (a) The energy levels of the specific ion class that is selected and the involved three laser beams. During ion class selection, all the other ion classes have a hyperfine ground state that is not addressed with any of the lasers. As a result, with all three beams turned on, all the other ion classes are optically pumped and are, therefore, rendered "dark". (b) An example 14 MHz spectral-trough that is burned by any one of the beams. Such spectral-troughs are achieved by scanning the beam frequency during the spectral-hole burning process. (c) The experimental timing diagram (not to scale). During ion class selection, the three lasers are turned on and their frequencies are continually scanned over about 10 MHz. Optical pumping followed by state initialization produces ions that are within a certain frequency range in the $|\pm 1/2\rangle$ ground hyperfine state. This creates a narrow, $\approx$ 1 MHz wide, absorption resonance for the probe laser beam (i.e., effectively an "ultracold" ensemble is created), which we then use for slow-light and EIT experiments. The first three steps (ion class selection, optical pumping, and state-initialization) last about 3 s each. For the final step, we use μs-long pulses.

probe laser beam (i.e., effectively an "ultracold" ensemble is created). The second and third steps also last for about 3 s each. In the fourth and final step, we use the selected, optically pumped, and appropriately initialized ensemble for linear and nonlinear optics experiments. Here, we use short, μs-time-scale pulses. For linear experiments, we turn on only the probe

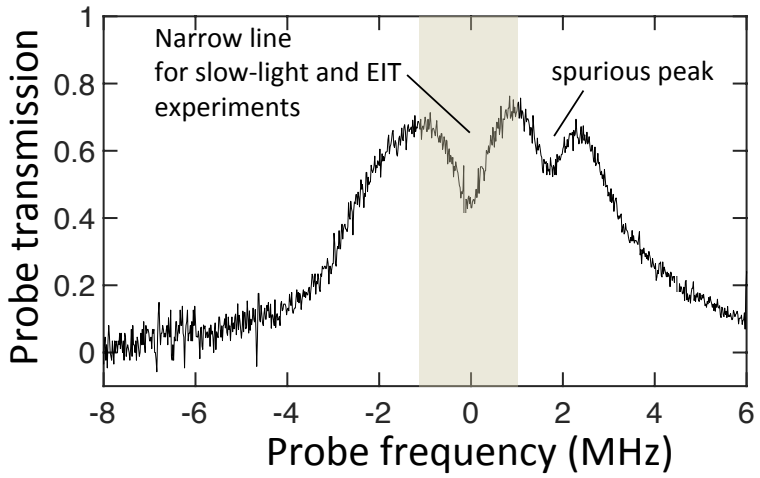

FIG. 5: The absolute transmission of a weak probe laser beam through the crystal. This measurement is performed with the coupling laser off and after the ion class selection, optical pumping and state initialization steps. A 1 MHz absorption resonance with an optical depth of about 0.3 is created. The data also shows a spurious peak, which may be a result of an currently unidentified splitting of the hyperfine levels.

laser beam and investigate its absorption and time delay through the sample. For EIT, the coupling laser is also turned on in addition to the probe beam.

An example narrow absorption resonance that is produced for the probe laser beam is shown in Fig. 5. Here, the transmission of a weak probe laser through the crystal is measured (with the coupling laser turned off), after ion class distillation and optical pumping steps as discussed above. A 1 MHz absorption resonance with an optical depth of about 0.3 is created. This data is taken using a 40 μs long probe laser pulse, and the laser frequency is chirped during the pulse so that the whole frequency response is obtained in a single experiment. The data shown is an average over five experiments. The data of Fig. 5 also shows a spurious peak, which may be a result of a currently unidentified splitting of the hyperfine levels.

VI. SLOW-LIGHT AND EIT

We will now discuss our slow-light and EIT experiments. Using the selected ensemble, we have been able to observe linear group velocity reduction. Figure 6(a) shows the propagation of a 1/4 μs-long probe laser pulse whose frequency is detuned by 0.8 MHz from the peak of the narrow absorption resonance. In addition to significant reshaping of the pulse, we observe a group delay of 127 ns while propagating through the crystal. This group delay corresponds to a group velocity of $v_g = 7.8 \times 10^4$ m/s, which is 3800 times slower than the speed of light in free space. Note that this group delay is not that which is typically associated with EIT. Rather, it is due to the large dispersion due to the narrow absorption profile as shown in Fig. 5. We also performed this slow-light experiment using longer 5 μs-long probe pulses. As shown in Fig. 6(b), we observe significantly larger group delay of 224 ns, corresponding to a substantially slower pulse. The slower group velocity is most likely due to the narrower bandwidth of the longer pulse, which also results in much less distortion and pulse shaping, compared to the data of Fig. 6(a). To our knowledge, this is the first observation of group velocity reduction using interaction with the magnetic field of light.

For EIT, with the ions selected and initialized to the $|\pm 1/2\rangle$ hyperfine state, we turn on both probe and coupling laser pulses. To allow adiabatic preparation of the dark state, we turn on the coupling laser beam before the probe, and then measure the transmission of a weak probe laser pulse through the crystal. Similar to the transmission experiment of Fig. 5, we use a 40-μs-long probe laser pulse, and chirp the probe frequency during the pulse so that the whole frequency response is obtained in a single experiment. Figure 7 shows normalized probe transmission with and without the coupling laser beam. As expected, with the coupling laser, there is a splitting of the line (Autler-Townes splitting), with slight but observable increase in the transmission at line center. The solid red-line is a fit to the data points using the well-known EIT-lineshape for the susceptibility [30]:

$$\chi_M = \frac{N\mu^2}{\epsilon_0 \hbar} \frac{\delta\omega + i\gamma}{(\delta\omega + i\gamma + i\Gamma/2)(\delta\omega + i\gamma) - |\Omega_C|^2} \quad . \tag{1}$$

Here, we have taken the coupling laser beam to be exactly resonant between the relevant levels. Γ is the population decay rate of the excited level, and γ is the dephasing rate between the two ground hyperfine states. The quantity $\delta\omega$ is the frequency detuning of the probe laser beam from the excited level (which is also the two photon Raman detuning since

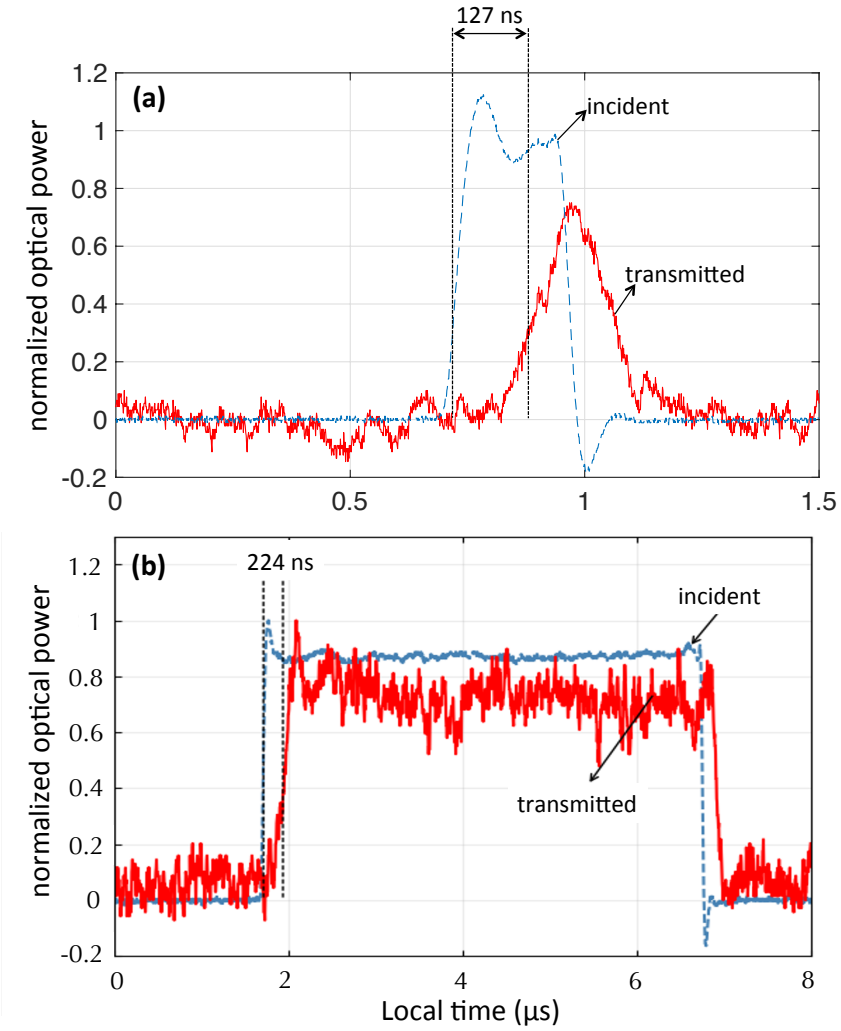

FIG. 6: (a) The propagation of a 1/4 μs-long probe laser pulse whose frequency is detuned by 0.8 MHz from the narrow absorption resonance. We observe a group delay of 127 ns while propagating through the crystal, corresponding to a group velocity of $v_g = 7.8 \times 10^4$ m/s$\approx c/3800$. (b) The propagation of a 5 μs-long probe pulse with the same detuning. We observe less distortion, but a longer group delay, corresponding to a slower group velocity. This is likely due to the narrower bandwidth of the longer pulses.

the coupling laser is assumed to be resonant), and Ω_C is the Rabi frequency of the coupling laser beam. The best fit gives a coupling laser Rabi frequency of $\Omega_C = 2\pi \times 350$ kHz and a Raman dephasing rate of $\gamma = 2\pi \times 150$ kHz. The physical mechanism for this large Raman dephasing rate is currently an open question.

The bottom plot in Fig. 7 is the calculated change in the real part of the magnetic susceptibility due to EIT. We can modify the real part of χ_M by $\approx 10^{-6}$. These experiments extend previous EIT and quantum coherence experiments that were observed in rare-earth doped crystals [50–54] to interactions with the magnetic field of light.

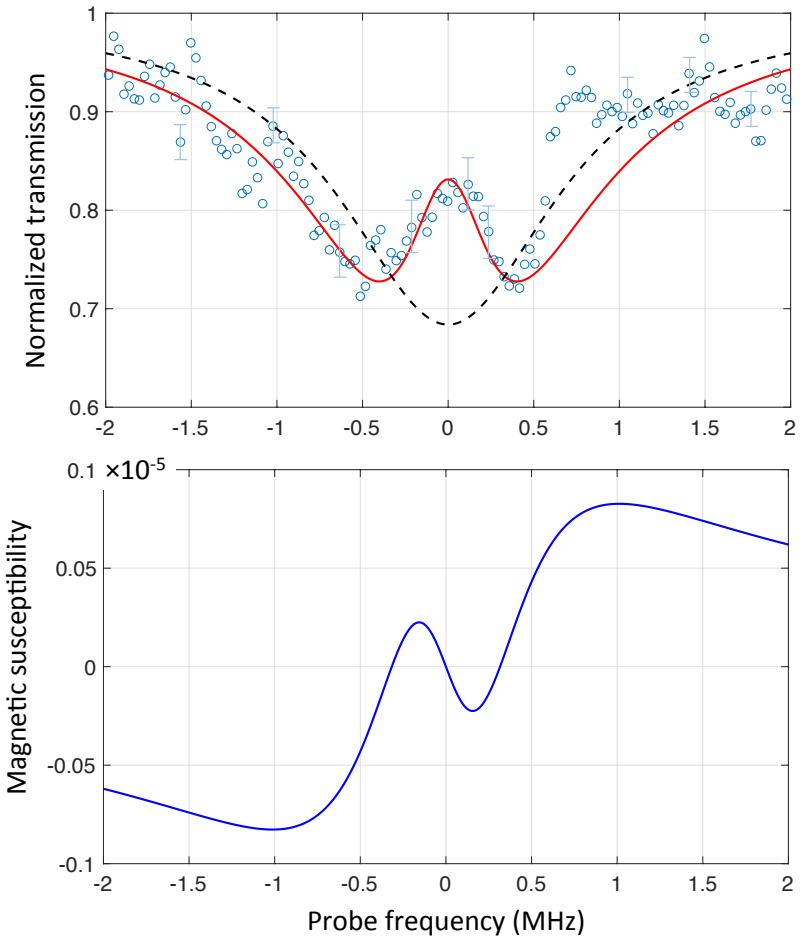

FIG. 7: Normalized probe transmission with the coupling laser beam (shown as data points) and without it (shown as a dashed line). With the coupling laser, there is splitting of the line (Autler-Townes splitting), with slight but observable increase in the transmission at line center. The solid red line is a fit to the data points using the well-known EIT-lineshape. The bottom plot is the calculated real part of the magnetic susceptibility under the conditions of EIT.

The data of Fig. 7 is obtained using a coupling laser power of 23 mW (beam intensity

of 723 W/cm^2 at the focus). Using the inferred value of the coupling laser Rabi frequency from the fit ($\Omega_C = 2\pi \times 350$ kHz), we calculate the magnetic-dipole matrix element for the specific hyperfine transition to be $\mu = (0.10 \pm 0.01)\mu_B$ (μ_B is the Bohr magneton). This is reasonably consistent with the hyperfine-averaged matrix element measurements of our previous Rabi flopping experiments [40].

VI. CONCLUSIONS

We studied the $^7F_0 \rightarrow {}^5D_1$ magnetic-dipole transition in the $4f$ shell of europium ions at a wavelength of 527.5 nm. We first demonstrated spectral hole burning, ion class selection and state initialization under the inhomogeneous profile. This allowed us to produce MHz-wide, magnetic-dipole optical absorption resonances with multiple stable ground hyperfine states. Using these narrow lines, we demonstrated slow light and EIT. EIT using a magnetic-dipole transition has been observed before, but only in a vapor (within the context of atomic parity violation experiments) [55]. All EIT experiments in solids to date used interaction with the electric field to increase transmission of a laser beam and therefore modified the electric susceptibility. In our experiments, we used the interaction with the magnetic-field and modified the magnetic susceptibility.

One of the main limitations of our current experiment is the absolute frequency and phase noise on our laser beams. The whole ion-class selection, optical pumping, and EIT experimental cycle takes a fraction of a minute, and it is critical for the absolute frequency of the laser to not drift much during the cycle. We have found that our experimental results depend critically on the quality of the lock of the ECDL to the ULE cavity. Due to this frequency and phase noise limitation, we were not able to observe coherent control of the group velocity of light by changing the intensity of the coupling laser beam. Improving the absolute linewidth of our laser system will likely result in better EIT data, and also will allow us to observe other quantum coherence effects such as stopped and backward light [56–59]. On a related note, more available optical power in the coupling laser beam would result in a larger coupling Rabi frequency, allowing for a deeper and wider EIT transmission window.

To our knowledge, this is the first experiment to demonstrate control of the magnetic susceptibility, and therefore the permeability, in a bulk crystal. As mentioned in the intro-

duction, one immediate application of this work is to the field of negative index materials. The modification of the permeability that we demonstrate in this article is not currently sufficient to achieve a negative refractive index. We are able to achieve a magnetic susceptibility (and therefore the permeability) at the level of $\chi_M \approx 10^{-5}$. However, there are many avenues for future research to improve these results. For example, using stronger magnetic dipole transitions and higher ionic densities (with higher doping concentrations), it will likely be possible to increase the magnetic susceptibility significantly. Similarly, decreasing the inhomogeneous broadening can lead to much higher effective densities, and therefore larger modifications of the permeability. It is known that repeated re-crystallization and therefore purification of the host material can lead to significant narrowing in inhomogeneous linewidth [34]. Some special host crystals are known to provide a near-strain free environment, producing inhomogeneous lines as narrow as 10 MHz. Yet another narrowing mechanism is due to the strong hyperfine interaction of the rare-earth ion. In these systems, the hyperfine interaction defines a quantization axis, which makes the strain-shift terms off-diagonal, thereby reducing their effectiveness. We note that inhomogeneous broadening can also be overcome using laser-based methods. For example, it might be possible to utilize the suggestion of Ref. [60] and compensate for the frequency shifts due to the broadening process with an equal and opposite shift caused by an intense Stark-shift laser beam.

The extension of this work to magnetic-dipole transitions at shorter wavelengths would be interesting and exciting. Current structured metamaterials are limited to a shortest wavelength near the middle of the visible range of the spectrum [31, 61, 62]. Rare earth ions could provide a unique environment to obtain strong magnetic response in the ultraviolet region of the spectrum. For example, we have recently identified a strong magnetic-dipole transition at a wavelength of 282 nm in terbium (Tb^{+3}) [26].

VII. ACKNOWLEDGEMENTS

This work was supported by Air Force Office of Scientific Research (AFOSR) and Wisconsin Alumni Research Foundation (WARF). We thank Nick Brewer and Zach Simmons for their contributions in the early stages of this project. We also would like to thank Josh Karpel and David Gold for many helpful discussions.

[1] V. G. Veselago, *The Electrodynamics of Substances with Simultaneously Negative Values of ϵ and μ*, Sov. Phys. Usp. **10**, 509 (1968).

[2] J. B. Pendry, *Negative Refraction Makes a Perfect Lens*, Phys. Rev. Lett. **85**, 3966 (2000).

[3] D. R. Smith and N. Kroll, *Negative Refractive Index in Left-Handed Materials*, Phys. Rev. Lett. **85**, 2933 (2000).

[4] S. Foteinopoulou, E. N. Economou, and C. M. Soukoulis, *Refraction in Media with a Negative Refractive Index*, Phys. Rev. Lett. **90**, 107402 (2003).

[5] J. B. Pendry, A. Aubry, D. R. Smith, and S. A. Maier, *Transformation Optics and Subwavelength Control of Light*, Science **337**, 549 (2012).

[6] R. A. Shelby, D. R. Smith, and S. Shultz, *Experimental Verification of a Negative Index of Refraction*, Science **292**, 77 (2001).

[7] A. H. Houck, J. B. Brock, and I. L. Chuang, *Experimental Observations of a Left-Handed Material That Obeys Snells Law*, Phys. Rev. Lett. **90**, 137401 (2003).

[8] H. J. Lezec, J. A. Dionne, H. A. Atwater, *Negative Refraction at Visible Frequencies*, Science **316**, 430 (2007).

[9] S A. Ramakrishna, *Physics of Negative Refractive Index Materials*, Rep. Prog. Phys. **68**, 449 (2005)

[10] S. Linden, C. Enkrich, M. Wegener, J. Zhou, T. Koschny, and C. M. Soukoulis, *Magnetic Response of Metamaterials at 100 Terahertz*, Science **306**, 1351 (2004).

[11] H. T. Chen, A. J. Taylor, and N. Yu, *A Review of Metasurfaces: Physics and Applications*, Rep. Prog. Phys. **79**, 076401 (2016).

[12] L. Ferraria, C. Wu, D. Lepaged, X. Zhang, and Z. Liua, *Hyperbolic Metamaterials and Their Applications*, Prog. in Quant. Electronics **40**, 1 (2015).

[13] M. Lapine, I. V. Shadrivov, and Y. S. Kivshar, *Colloquium: Nonlinear metamaterials*, Rev. Mod. Phys. **86**, 1093 (2014).

[14] P. Cheben, R. Halir, J. H. Schmid, H. A. Atwater, and D. R. Smith, *Subwavelength Integrated Photonics*, Nature **560**, 572 (2018).

[15] Q. Zhao J. Zhou, F. Zhang, and D. Lippens, *Mie Resonance-Based Dielectric Metamaterials*, Materials Today **12**, 60 (2009).

[16] P. Moitra, Y. Yang, Z. Anderson, I. I. Kravchenko, D. P. Briggs, and J. Valentine, *Realization of An All-Dielectric Zero-Index Optical Metamaterial*, Nat. Photonics **7**, 791 (2013).

[17] S. Jahani and Z. Jacob, *All-dielectric Metamaterials*, Nat. Nanotechnology DOI:10.1038 (2016).

[18] M. O. Oktel and O. E. Mustecaplioglu, *Electromagnetically Induced Left-Handedness in a Dense Gas of Three-Level Atoms*, Phys. Rev. A **70**, 053806 (2004).

[19] Q. Thommen and P. Mandel, *Electromagnetically Induced Left Handedness in Optically Excited Four-Level Atomic Media*, Phys. Rev. Lett. **96**, 053601 (2006).

[20] P. P. Orth, R. Hennig, C. H. Keitel, and J. Evers, *Negative Refraction with Tunable Absorption in an Active Dense Gas of Atoms*, N. J. of Physics **15**, 013027 (2013).

[21] A. P. Fang, W. Ge, M. Wang, F. Li, and M. S. Zubairy, *Negative Refraction Without Absorption via Quantum Coherence*, Phys. Rev. A **93**, 023822 (2016).

[22] J. Kästel, M. Fleischhauer, S. F. Yelin, and R. L. Walsworth, *Tunable Negative Refraction without Absorption via Electromagnetically Induced Chirality*, Phys. Rev. Lett. **99**, 073602 (2007).

[23] J. Kästel, M. Fleischhauer, S. F. Yelin, and R. L. Walsworth, *Low-loss Negative Refraction by Laser-induced Magnetoelectric Cross Coupling*, Phys. Rev. A **79**, 063818 (2009).

[24] D. E. Sikes and D. D. Yavuz, *Negative Refraction with Low Absorption using Raman Transitions with Magneto-Electric Coupling*, Phys. Rev. A **82**, 011806(R) (2010).

[25] D. E. Sikes and D. D. Yavuz, *Negative Refraction Using Raman Transitions and Chirality*, Phys. Rev. A **84**, 053836 (2011).

[26] D. D. Yavuz and Z. N. Buckholtz, *Negative Index Materials Using Atomic Transitions: Progress and Challenges*, Advances in At. Mol. Opt. Phys. **67**, 429 (2018).

[27] X. A. Shen and R. Kachru, $^7F_0 \rightarrow ^5D_1$ *Transition in Eu:YSO*, J. Opt. Soc. Am. B **11**, 591 (1994).

[28] M. O. Scully and M. S. Zubairy, *Quantum Optics* (Cambridge University Press, Cambridge, 1997).

[29] S. E. Harris, *Electromagnetically Induced Transparency*, Phys. Today **50**, No. 7, 36 (1997).

[30] M. Fleischhauer, A. Imamoglu, and J. P. Marangos, *Electromagnetically Induced Transparency: Optics in Coherent Media*, Rev. Mod. Phys. **77**, 633 (2005)

[31] R. S. Penciu, M. Kafesaki, Th. Koschny, E. N. Economou, and C. M. Soukoulis, *Magnetic*

Response of Nanoscale Left-Handed Metamaterials, Phys. Rev. B **81**, 235111 (2010).

[32] B. G. Wybourne, *Spectroscopic Properties of Rare-Earths* (John Wiley & Sons, 1965).

[33] K. N. R. Taylor and M. I. Darby, *Physics of Rare Earth Solids* (Chapman and Hall, 1972).

[34] R. M. Macfarlane, *High-Resolution Laser Spectroscopy of Rare-Earth Doped Insulators: A Personal Perspective*, J. Lumin. **100**, 1 (2002).

[35] P. S. Peijzel, A. Meijerink, R. T. Wegh, M. F. Reid, and G. W. Burdick, *A Complete* $4f$ *Energy Level Diagram for All Trivalent Lanthanide Ions*, J. Solid State Chem. **178**, 448 (2005).

[36] G. S. Ofelt, *Structure of the* f^6 *Configuration with Application to Rare-Earth Ions*, J. Chem. Phys. **38**, 2171 (1962).

[37] G. S. Ofelt, *Intensities of Crystal Spectra of Rare-Earth Ions*, J. Chem. Phys. **37**, 511 (1962).

[38] G. H. Dieke and H. M. Crosswhite, *The Spectra of the Doubly and Triply Ionized Rare Earths*, Applied Optics **2**, 675 (1963).

[39] M. Kasperczyk, S. Person, D. Ananias, L. D. Carlos, and L. Novotny, *Excitation of Magnetic Dipole Transitions at Optical Frequencies*, Phys. Rev. Lett. **114**, 163903 (2015).

[40] N. R. Brewer, Z. N. Buckholtz, Z. J. Simmons, E. A. Mueller, and D. D. Yavuz, *Coherent Magnetic Response at Optical Frequencies Using Atomic Transitions*, Phys. Rev. X **7**, 011005 (2017).

[41] A. Vaskin *et al.*, *Manipulation of Magnetic Dipole Emission from* Eu^{+3} *with Mie-Resonant Dielectric Metasurfaces* Nano Lett. **19**, 1015 (2019).

[42] S. L. Oliviera and S. C. Rand, *Intense Nonlinear Magnetic Dipole Radiation at Optical Frequencies: Molecular Scattering in a Dielectric Liquid*, Phys. Rev. Lett. **98**, 093901 (2007).

[43] S. C. Rand, W. M. Fisher, and S. L. Oliviera, *Optically Induced Magnetization in Homogeneous, Undoped Dielectric Media*, J. Opt. Soc. Am. B **25**, 1106 (2008).

[44] A. A. Fisher, E. F. C. Dreyer, A. Chakrabarty, and S. C. Rand, *Optical Magnetization, Part I: Experiments on Radiant Optical Magnetization in Solids*, Opt. Express **24**, 26064 (2016).

[45] A. A. Fisher, E. F. C. Dreyer, A. Chakrabarty, and S. C. Rand, *Optical Magnetization, Part II: Theory of Induced Optical Magnetism*, Opt. Express **24**, 26064 (2016).

[46] M. Nilsson, L. Rippe, N. Ohlsson, T. Christiansson, and S. Kroll, *Initial Experiments Concerning Quantum Information Processing in Rare-Earth-Ion Doped Crystals*, Phys. Scr. T **T102**, 178 (2002).

[47] M. Nilsson, L. Rippe, S. Kroll, R. Klieber, and D. Suter, *Hole-burning Techniques for Iso-*

lation and Study of Individual Hyperfine Transitions in Inhomoheneously Broadened Solids Demonstrated in Pr:YSO Phys. Rev. B **70**, 214116 (2004).

[48] F. Konz, Y. Sun, C. W. Thiel, R. L. Cone, R. W. Equall, R. L. Hutcheson, and R. M. Macfarlane, *Temperature and Concentration Dependence of Optical Dephasing, Spectral-Hole Lifetime, and Anisotropic Absorption in* Eu^{+3}*:*Y_2SiO_5, Phys. Rev. B **68**, 085109 (2003).

[49] B. Lauritzen, N. Timoney, N. Gisin, M. Afzelius, H. de Rietmatten, Y. Sun, R. M. Macfarlane, and R. L. Cone, *Spectroscopic Investigations of* Eu^{+3}*:*Y_2SiO_5 *for Quantum Memory Applications*, Phys. Rev. B **85**, 115111 (2012).

[50] B. S. Ham, P. R. Hemmer, and M. S. Shahriar, *Efficient Electromagnetically Induced Transparency in a Rare-earth Doped Crystal*, Opt. Commun. **144**, 227 (1997).

[51] A. V. Turukhin, V. S. Sudarshanam, M. S. Shahriar, J. A. Musser, B. S. Ham, and P. R. Hemmer, *Observation of Ultraslow and Stored Light Pulses in a Solid*, Phys. Rev. Lett. **88**, 023602 (2001).

[52] J. Klein, F. Beil and T. Halfmann, *Rapid Adiabatic Passage in a* Pr^{+3}*:*Y_2SiO_5 *Crystal*, J. Phys. B: At. Mol. Opt. Phys. **40**, 345 (2007).

[53] J. Klein, F. Beil, and T. Halfmann, *Experimental Investigations of Stimulated Raman Adiabatic Passage in a Doped Solid*, Phys. Rev. A **78**, 033416 (2008).

[54] H. Q. Fan, K. H. Kagalwala, S. V. Polyakov, A. L. Migdall, and E. A. Goldschmidt, *Electromagnetically Induced Transparency in Inhomogeneously Broadened Solid Media*, Phys. Rev. A **99**, 053821 (2019).

[55] A. D. Cronin, R. B. Warrington, S. K. Lamoreaux, and E. N. Fortson, *Studies of Electromagnetically Induced Transparency in Thallium Vapor and Possible Utility for Measuring Atomic Parity Nonconservation*, Phys. Rev. Lett. **80**, 3719 (1998).

[56] M. Fleischhauer and M. D. Lukin, *Dark State Polaritons in Electromagnetically Induced Transparency*, Phys. Rev. Lett. **84**, 5094 (2000).

[57] D. F. Phillips, A. Fleischhauer, A. Mair, R. L. Walsworth, and M. D. Lukin, *Storage of Light in Atomic Vapor*, Phys. Rev. Lett. **86**, 783 (2001).

[58] N. B. Phillips, A. V. Gorshkov, and I. Novikova, *Optimal Light Storage in Atomic Vapor*, Phys. Rev. A **78**, 023801 (2008).

[59] G. M. Gehring, A. Schweinsberg, C. Barsi, N. Kostinski, and R. W. Boyd, *Observation of Backward Pulse Propagation Through a Medium with a Negative Group Velocity*, Science **312**,

895 (2006).

[60] D. D. Yavuz, N. R. Brewer, J. A. Miles, and Z. J. Simmons, *Suppression of Inhomogeneous Broadening Using the AC Stark Shift*, Phys. Rev. A **88**, 063836 (2013).

[61] S. Xiao, U. K. Chettiar, A. V. Kildishev, V. P. Drachev, and V. M. Shalaev, *Yellow-light Negative-Index Metamaterials*, Opt. Lett. **34**, 3478 (2009).

[62] Y. Liang, Z. Yu, N. Ruan, Q. Sun, and T. XU, *Freestanding Optical Negative-Index Metamaterials of Green Light*, Opt. Lett. **42**, 3239 (2017).